J. Fluid Mech. (2002), *vol.* 468, *pp.* 153–177.
DOI: 10.1017/S0022112002001635 Printed in the United Kingdom

A magnetohydrodynamic chaotic stirrer

By MINGQIANG YI, SHIZHI QIAN AND HAIM H. BAU†

Department of Mechanical Engineering and Applied Mechanics, University of Pennsylvania, Philadelphia, PA 19104-6315, USA

(Received 11 July 2001 and in revised form 8 May 2002)

A magnetohydrodynamic (MHD) stirrer that exhibits chaotic advection is investigated experimentally and theoretically. The stirrer consists of a circular cavity with an electrode (C) deposited around its periphery. Two additional electrodes (A) and (B) are deposited eccentrically inside the cavity on the bottom. The cavity is positioned in a uniform magnetic field that is parallel to the cylinder's axis, and it is filled with a weak electrolyte solution. Fluid motion is induced in the cavity by applying a potential difference across a pair of electrodes. A closed-form, analytical solution is derived for the MHD creeping flow field in the gap between the two eccentric cylinders. A singular solution is obtained for the special case when the size of the inner electrode shrinks to a point. Subsequently, passive tracers' trajectories are computed when the electric potential differences are applied alternately across electrodes AC and BC with period T. At small periods T, the flow is regular and periodic in most of the cavity. As the period increases, so does the complexity of the motion. At relatively large periods, the passive tracer experiences global chaotic advection. Such a device can serve as an efficient stirrer. Since this device has no moving parts, it is especially suitable for microfluidic applications. This is yet another practical example of a modulated, two-dimensional Stokes flow that exhibits chaotic advection.

1. Introduction

In recent years, there has been a growing interest in developing minute chemical and biological laboratories and reactors. Often it is necessary to propel fluids from one part of a device to another, control the fluid motion, mix, and separate fluids. In microdevices, these tasks are far from trivial. Typically, electrostatic forces are being used to move liquids around. These forces usually induce very low flow rates, require the use of high electrical potentials, and may cause significant heating of the solution. The use of electromagnetic forces presents an interesting and flexible means of manipulating liquids in microfluidic devices and systems. The only requirement is that the liquid be at least slightly conductive. This requirement is met by many biological solutions.

The application of electromagnetic forces to pump, confine and control fluids is by no means new. To date, magnetohydrodynamics (MHD) has mostly been used to pump and control highly conducting fluids such as liquid metals and ionized gases and to study ionospheric/astrophysical plasmas (i.e. Woodson & Melcher 1969; Davidson 2001). The potential use of electromagnetic forces in microdevices has attracted much less attention. Recently, Jang & Lee (2000), Lemoff & Lee (2000), and Zhong, Yi & Bau (2001) have constructed MHD micro-pumps on silicon and ceramic

† Author to whom correspondence should be addressed: bau@seas.upen.edu

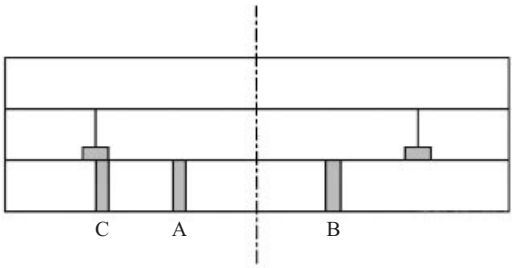

FIGURE 1. A schematic depiction of a magnetohydrodynamic stirrer. The dark segments denote the electrodes. Electrodes A and B are located on the cavity's bottom. Electrode C is shaped like a disk and surrounds the cavity. The cavity is filled with saline solution.

substrates and demonstrated that these pumps are able to move liquids around in micro-conduits. MHD can be used not only for the purpose of pumping fluids, but also to control fluid flow in networks of conduits and to induce secondary complex flows that may be beneficial for stirring and mixing. For example, Bau, Zhong & Yi (2001) deposited an array of transverse electrodes on the bottom of a conduit. The electrodes were connected alternately to two terminals of a DC power supply. As a result, electric currents were induced in opposite directions between adjacent pairs of electrodes. The interaction between these currents and a uniform magnetic field perpendicular to the bottom of the conduit led to the formation of Lorentz forces in opposing directions between adjacent pairs of electrodes. This, in turn, led to the formation of cellular convection. This motion can be used to deform and stretch material interfaces and enhance mixing. Since we have the freedom to pattern the electrodes in any desired way, one can envision the feasibility of generating 'local' volumetric forces to direct the flow in 'wall-less' conduits.

In this paper, we take the above ideas one step further and design a stirrer that exhibits chaotic advection. The stirrer consists of a circular cavity with an electrode C deposited along its periphery. Two additional electrodes, A and B, are deposited on the cavity bottom. See figure 1 for a schematic description of the device. The cavity is filled with a weakly conducting liquid such as saline solution, and it is positioned in a uniform magnetic field that is parallel to the cavity axis. Such a magnetic field can be generated, for example, by a permanent magnet or an electromagnet. When a potential difference is imposed between the two electrodes (A) and (C), say, an electric current flows between them. The interaction between this current and the magnetic field results in Lorentz forces that, in turn, induce counterclockwise (say) flow circulation in the cavity centred next to electrode A. Subsequently, when the potential difference is switched from electrode pair AC to electrode pair BC, depending on the polarity of the electrodes, one can induce either a counterclockwise or clockwise circulatory pattern centred next to electrode B. Using Aref's (1984) terminology, we refer to each electrode pair as an agitator. We operate the device by alternately engaging electrode pairs AC and BC with a period T. The fluid viscosity is sufficiently high that transient effects can be neglected and the instantaneous Eulerian flow field can be described as a Stokes flow. We show that the trajectories of passive tracers may be quite complicated. As the period of the alternations T increases so does the complexity of the tracer motion.

The design of the above-described MHD stirrer was inspired by Aref's (1984) study of the inviscid blinking vortex pair. Each pair of electrodes in our device induces circulatory motion. Aref (1984) considered, however, a highly idealized, inviscid sys-

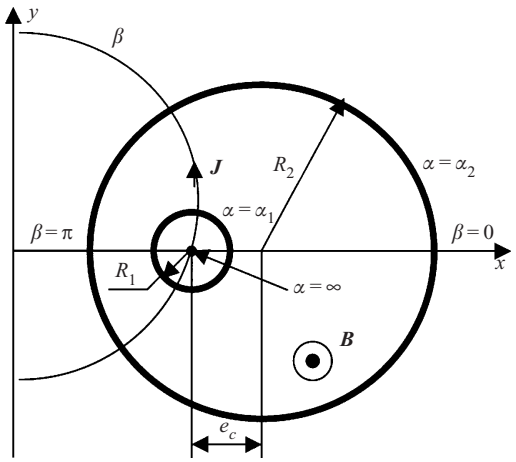

FIGURE 2. A liquid-filled two-dimensional cavity confined between two eccentric cylinders of radii R_1 and R_2 and eccentricity e_c. Both cylinder surfaces are metalized to form electrodes. A uniform magnetic field, $\boldsymbol{B}$, is directed out of the page. The figure depicts both the Cartesian (x, y) and the bi-cylindrical (α, β) co-ordinate systems. The coordinates $\alpha = \alpha_1$ and $\alpha = \alpha_2$ coincide, respectively, with the inner and outer cylinders.

tem. In contrast, our system is easily constructed and implemented in an experiment. Nevertheless, there are many qualitative similarities between the Lagrangian motion observed in our viscous system and the motion in the inviscid system studied by Aref. Our paper is also related to the studies of chaotic advection in two-dimensional, time-dependent Stokes flows induced by two rotating eccentric cylinders (i.e. Aref & Balachandar 1986; Chaiken *et al.* 1986, 1987). We provide here yet another practical example of chaotic advection in a simple flow system. Since the device does not include any moving parts, it is particularly appropriate for use as a stirrer in microfluidic devices.

The paper is organized as follows: first, we derive an expression for the MHD flow field between two eccentric cylinders; next we obtain asymptotic expressions for the case when the radius of the inner cylinder shrinks to zero. In both cases, one can obtain a closed-form description of the flow field. Subsequently, using a quasi-static approximation, we compute the flow field and the trajectories of the passive tracers when the two pairs of electrodes AC and BC are activated alternately. Finally, the theoretical results are qualitatively compared with experimental observations. Although the mathematical model consists of a very idealized description of the physical set-up, the experiment demonstrates that the ideas described in this paper can, indeed, be implemented in practice.

2. Mathematical model

We focus our attention on low-Reynolds-number viscous-dominated (creeping) flows. We start by developing an analytic solution for two-dimensional MHD flow in a cavity confined between two eccentric cylinders.

2.1. *MHD flow between two eccentric cylinders*

Consider an eccentric annulus (figure 2). R_1 and R_2 denote, respectively, the radii of the inner and outer cylinders. Without loss of generality, we position both cylinder

centres on the x-axis. The distance between the cylinder centres is the eccentricity e_c. The cavity is placed in a uniform static magnetic field of flux density $\boldsymbol{B} = B\hat{\boldsymbol{e}}_z$ directed in the (z) direction, which is parallel to the axes cylinders. We use bold letters to denote vectorial quantities. The cavity is filled with a weak electrolyte solution of electrical conductivity σ and viscosity μ. The cylinder surfaces in contact with the liquid are metallized to form two electrodes, C and A. Potentials V_1 and V_2 are, respectively, imposed on the surfaces of the inner (A) and outer (C) electrodes. The potential difference, $(\Delta V = V_1 - V_2)$, induces a current of density $\boldsymbol{J} = J_x\hat{\boldsymbol{e}}_x + J_y\hat{\boldsymbol{e}}_y$. More specifically, Ohm's law for a moving conductor of conductivity σ in a magnetic field is:

$$\boldsymbol{J} = \sigma(\boldsymbol{E} + \boldsymbol{u} \times \boldsymbol{B}) = \sigma(-\nabla V + \boldsymbol{u} \times \boldsymbol{B}). \tag{1}$$

In the above, $\hat{\boldsymbol{e}}_i$ is a unit vector in the i-direction; $\boldsymbol{u}$ is the fluid velocity vector; $\boldsymbol{E}$ is the electric field, and V is the electric potential. The interaction between the electric current and the magnetic field generates a (volumetric) Lorentz force of density, $\boldsymbol{J} \times \boldsymbol{B}$. We assume that the flow is two-dimensional and incompressible. The momentum equation is

$$\rho\frac{\mathrm{D}\boldsymbol{u}}{\mathrm{D}t} = \boldsymbol{J} \times \boldsymbol{B} - \nabla p + \mu\nabla^2\boldsymbol{u}, \tag{2}$$

where $\boldsymbol{u}$ is the velocity vector; t is time; p is the pressure; and ρ is the density. We non-dimensionalize equation (2) using R_2 as the length scale; $U = \sigma\Delta V B R_2/[\mu(\alpha_1 - \alpha_2)]$ as the velocity scale; the period T^* of the alternations in the electric field as the time scale; $\sigma\Delta V B/(\alpha_1 - \alpha_2)$ as the pressure scale; and ΔV as the electric potential scale. In the above, α_1 and α_2 are bi-cylindrical coordinates that we introduce later in this section. The dimensionless momentum equation is

$$St^2\frac{\partial\boldsymbol{u}}{\partial t} = (-(\alpha_1 - \alpha_2)\nabla V + Ha^2\boldsymbol{u} \times \hat{\boldsymbol{e}}_z) \times \hat{\boldsymbol{e}}_z - \nabla p + \nabla^2\boldsymbol{u}. \tag{3}$$

In the above, we neglected advection, assuming that the Reynold number ($Re = UR_2/\nu$) is small. The Stanton number, $St = R_2/\sqrt{\nu T^*}$, is the ratio between the diffusion time and the forcing period. When $St \ll 1$, the flow can be assumed to be quasi-static, and the time-derivative can be neglected. We show in the Appendix that even when $St = O(1)$, the quasi-static approximation still gives a qualitatively reasonable description of the flow. Both these approximations are discussed in Landau & Lifshitz (1959, p. 91). $Ha = BR_2\sqrt{\sigma/\mu}$ is the Hartman number. When the liquid is a weak conductor of electricity such as in the case of saline solutions, the Hartman number is small and the term $\boldsymbol{u} \times \boldsymbol{B}$ can be safely neglected. For example, in our case, $Ha \sim O(10^{-2})$.

For our particular geometry (figure 2), it is convenient to use the bi-cylindrical coordinates (α, β) (Moon & Spencer, 1971):

$$\alpha + \mathrm{i}\beta = \log\frac{y + i(x + a)}{y + i(x - a)}. \tag{4}$$

Briefly, the constant α coordinates represent a family of eccentric circles with their centres lying on the $y = 0$ axis. $\alpha = \infty$ is located at $x = a$ and $y = 0$. Constant β coordinates represent a second family of circles that are orthogonal to the constant α circles, and all of which pass through $(x, y) = (a, 0)$. In other words, the region confined between the inner cylinder, $(x - a\coth\alpha_1)^2 + y^2 = a^2/(\sinh^2\alpha_1)$, and the outer cylinder $(x - a\coth\alpha_2)^2 + y^2 = a^2/(\sinh^2\alpha_2)$, in the physical (x, y)-plane is mapped into the rectangle, $0 \leqslant \alpha_2 < \alpha < \alpha_1 \leqslant \infty$ and $-\pi < \beta < \pi$, in the (α, β)-plane. $\alpha = \alpha_1$

and $\alpha = \alpha_2$ define, respectively, the inner and the outer cylinders. Consistent with our non-dimensional scheme, we select $a = \sinh(\alpha_2)$.

The electric potential (V) satisfies Laplace's equation, $\nabla^2 V = 0$. Therefore, in the bi-cylindrical coordinate system, the dimensionless potential is

$$V = \frac{\alpha - \alpha_2}{\alpha_1 - \alpha_2}. \tag{5}$$

Consequently, the dimensional current density

$$\boldsymbol{J} \approx h \frac{\sigma}{R_2} \frac{V_1 - V_2}{\alpha_1 - \alpha_2} \hat{\boldsymbol{e}}_\alpha,$$

where

$$h = \frac{1}{a}(\cosh\alpha - \cos\beta). \tag{6}$$

The dimensional Lorentz force is

$$\boldsymbol{J} \times \boldsymbol{B} = h \frac{\sigma B}{R_2} \frac{V_1 - V_2}{\alpha_1 - \alpha_2} \hat{\boldsymbol{e}}_\beta,$$

and the dimensionless steady-state momentum equation becomes

$$h^{-1} \nabla^2 \boldsymbol{u} = \hat{\boldsymbol{e}}_\beta + \left(\frac{\partial p}{\partial \alpha} \hat{\boldsymbol{e}}_\alpha + \frac{\partial p}{\partial \beta} \hat{\boldsymbol{e}}_\beta \right). \tag{7}$$

In order to compute the flow field, it is convenient to work in terms of the stream function ψ. It satisfies the bi-harmonic equation, $\nabla^4 \psi = 0$, and admits a solution of the form (Jeffery 1922)

$$h\psi = (A_0 + B_0\alpha)\cosh\alpha + (C_0 + D_0\alpha)\sinh\alpha + (A_1\cosh 2\alpha + B_1 + C_1 \sinh 2\alpha + D_1\alpha)\cos\beta. \tag{8}$$

The corresponding expression for the pressure is

$$p = \frac{2}{a}(\beta(B_0 + D_1 - \tfrac{1}{2}a) + ((B_0 - 2C_1 + D_1)\cosh\alpha + (D_0 - 2A_1)\sinh\alpha)\sin\beta - (C_1\cosh(2\alpha) + A_1\sinh(2\alpha))\sin(2\beta)). \tag{9}$$

Since the pressure must be single-valued,

$$B_0 + D_1 = a/2. \tag{10}$$

Additionally, we need to satisfy no-slip and impermeability boundary conditions at the surfaces of the inner and outer cylinders. At the inner boundary ($\alpha = \alpha_1$), we require $\psi = \partial(h\psi)/\partial\alpha = 0$, or more explicitly,

$$\left.\begin{aligned} &(A_0 + B_0\alpha_1)\cosh\alpha_1 + (C_0 + D_0\alpha_1)\sinh\alpha_1 = 0 \\ &A\cosh 2\alpha_1 + B_1 + C_1\sinh 2\alpha_1 + D_1\alpha_1 = 0, \end{aligned}\right\} \tag{11}$$

$$\left.\begin{aligned} &(D_0 + A_0 + B_0\alpha_1)\sinh\alpha_1 + (B_0 + C_0 + D_0\alpha_1)\cosh\alpha_1 = 0 \\ &2A\sinh 2\alpha_1 + 2C_1\cosh 2\alpha_1 + D_1 = 0. \end{aligned}\right\} \tag{12}$$

Similarly, at the outer boundary ($\alpha = \alpha_2$), $\psi = C = \text{constant}$ and $\partial(h\psi)/\partial\alpha = (C/a)\sinh\alpha_2$, or

$$\left.\begin{aligned} &(A_0 + B_0\alpha_2)\cosh\alpha_2 + (C_0 + D_0\alpha_2)\sinh\alpha_2 = (C/a)\cosh\alpha_2, \\ &(A_1\cosh 2\alpha_2 + B_1 + C\sinh 2\alpha_2 + D_1\alpha_2) = -C/a, \end{aligned}\right\} \tag{13}$$

$$\left.\begin{aligned}&(D_0 + A_0 + B_0\alpha_2)\sinh\alpha_2 + (B_0 + C_0 + D_0\alpha_2)\cosh\alpha_2 = (C/a)\sinh\alpha_2,\\ &2A\sinh 2\alpha_2 + 2C_1\cosh 2\alpha_2 + D_1 = 0.\end{aligned}\right\} \quad (14)$$

The algebraic equations (10)–(14) were solved with *Mathematica* (Wolfram 1996) to obtain the various coefficients in closed form. Since the resulting expressions are lengthy, they are not reproduced here.

An example of the flow field between two eccentric cylinders is depicted in the Appendix (figure 15). The fluid circulates around the inner cylinder. There are no internal stagnation points. In this sense, the MHD flow in the gap between two eccentric cylinders is topologically different from the shear-flow induced when the inner cylinder rotates as in Aref & Balachandar (1986) and Chaiken *et al.* (1987).

In our envisioned application, the inner electrode A is not an actual cylinder and it does not restrict the flow. Although the electrode has a finite radius, for mathematical convenience we consider the limiting case of $R_1 \to 0$ or $\alpha_1 \to \infty$.

2.2. *Singular solution*

We consider the limiting case when, in the (x, y)-plane, the inner electrode is the point $(a, 0)$ and the outer electrode is the circle with radius R_2. In other words, we let $R_1 \to 0$ and $\alpha_1 \to \infty$. At the same time, to maintain finite current, we adjust the potential difference ΔV so that $\Delta V/(\alpha_1 - \alpha_2)$ remains finite. The dimensional current per unit height of the cylinder (I', A m^{-1}) is

$$I' = \int_{-\pi}^{\pi} J\frac{R_2}{h}\mathrm{d}\beta = \int_{-\pi}^{\pi} h\frac{\sigma}{R_2}\frac{\Delta V}{\alpha_1 - \alpha_2}\frac{R_2}{h}\mathrm{d}\beta = \frac{2\pi\sigma\Delta V}{\alpha_1 - \alpha_2}. \quad (15)$$

Accordingly, it is convenient to re-write the velocity scale as $I'BR_2/2\pi\mu$.†

Since ψ and the velocity components must be bounded as $\alpha \to \infty$, we require that $C_1 = -A_1, C_0 = -A_0$, and $D_0 = -B_0$. At the outer boundary, $\alpha = \alpha_2$, we apply the conditions $\psi = C =$ constant and $u = v = 0$. As before, $B_0 + D_1 = a/2$, and

$$\left.\begin{aligned}A_0 = (a\mathrm{e}^{-2\alpha_2} + a - 2a\alpha_2)/4, \quad B_0 = a/2, \quad B_1 = -\tfrac{1}{2}a\mathrm{e}^{-2\alpha_2}, \quad A_1 = D_1 = 0,\\ C = \tfrac{1}{2}a^2\mathrm{e}^{-2\alpha_2}.\end{aligned}\right\} \quad (16)$$

Thus, the stream function has the form

$$h\psi = (A_0 + B_0\alpha)\,\mathrm{e}^{-\alpha} + B_1\cos\beta. \quad (17)$$

At the outer cylinder ($\alpha = \alpha_2$), the stream function has the value $C = \frac{1}{2}a^2\,\mathrm{e}^{-2\alpha_2} = \frac{1}{8}(1 - e_c^2)^2$.

More conveniently, equation (17) can be rewritten using the two radial coordinates, r_1, and r_2, respectively, centred at $(a, 0)$ and $(-a, 0)$: $a = \frac{1}{2}(e_c^{-1} - e_c)$, $r_1^2 = (x-a)^2 + y^2$, and $r_2^2 = (x + a)^2 + y^2$. Accordingly,

$$\Psi(x, y) = \tfrac{1}{8}\left(r_1^2\left(1 + 2\log\left(\frac{r_2}{r_1}e_c\right)\right) - e_c^2 r_2^2 + (1 - e_c^2)^2\right), \quad (18)$$

where e_c is the eccentricity, and in non-dimensional units, the cavity radius is one. The outer cylinder is specified by

$$r_1^2 + r_2^2 = (r_2^2 - r_1^2)\frac{1 + e_c^2}{1 - e_c^2}. \quad (19)$$

† We are grateful to an anonymous reviewer for suggesting this velocity scale.

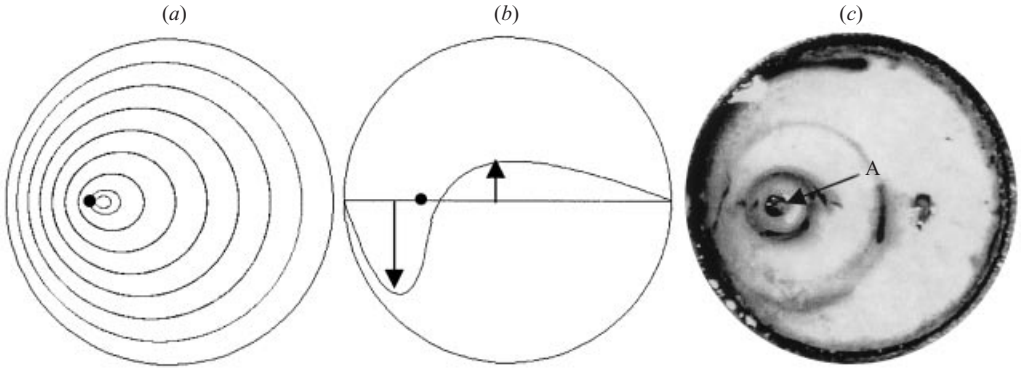

FIGURE 3. The flow field induced by one electrode pair. The radius of the outer cylinder $R_2 = 1$. $R_1 \to 0$ and the eccentricity $e_c = 1/2$. (*a*) Streamlines. (*b*) The vertical velocity $u_y(0, x)$ as a function of x. (*c*) A photograph of a flow visualization experiment.

Equation (18) can be recast in yet another form using radial coordinates (r, θ) with their origin at the cylinder centre:

$$\Psi(r,\theta) = (r^2 + 2e_c r\cos\theta + e_c^2)\log\left(\frac{e_c^2 r^2 + 2e_c r\cos\theta + 1}{r^2 + 2e_c r\cos\theta + e_c^2}\right) + (r^2 - e_c^2)(1 - e_c^2). \quad (20)$$

Equation (20) is a new singular solution for the Stokes equation in a cylinder.

Figure 3(*a*) depicts the streamlines computed with (18). The radius of the outer cylinder is one, the eccentricity $e_c = 1/2$, $a = 3/4$, and $\alpha_2 = \log(2) = 0.693$. The magnitude of the stream function at the outer cylinder's surface, $\alpha = \alpha_2$, is $C = 9/128$ and, at the inner electrode location, it is zero. The solid circle denotes the location of the electrodes. The streamlines form closed orbits, and the motion is regular. In contrast to the flow field induced by a rotlet (i.e. Meleshko & Aref 1996), with the exception of the centre of rotation, the MHD flow does not contain any stagnation points. Note than the centre of rotation is not at the electrodes but shifted to the right. We will discuss this shift in the location of the centre of rotation shortly.

Figure 3(*b*) depicts the vertical component of the velocity $u_y(x, 0)$ as a function of x. Note that the velocity is not zero at the electrodes. The velocity gradient on the electrode's left-hand side is larger than on its right-hand side. This is a direct result of the higher current density on the electrode's left-hand side (where the gap is narrower). Consequently, the vertical velocity immediately to the right of the electrode is directed downwards even though the Lorentz force at that location is directed upwards. In other words, the shift to the right of the point of zero velocity (and the centre of rotation) is caused by the competition between the Lorentz (upward) and the shear (downward) forces exerted by the fluid on the electrode's left-hand side. The centre of rotation is located at a radial distance of 0.41 units from the cylinder centre while the electrode is located at a radial distance of 0.5 units. More generally, the x-coordinate of the centre of rotation is $x_r = a(w + e_c)/(w - e_c)$, where w is a root of $w\log(w^2) = e_c(w^2 - 1)$. The centre of rotation $(x_r, 0)$ is a stagnation point.

Figure 3(*c*) depicts the results of flow visualization experiments. Dye was injected into the solution, and the figure shows the streaklines which under steady-state conditions coincide with the streamlines. The inner electrode is designated as A in figure 3(*c*). The experimental observations are in reasonable agreement with theoretical

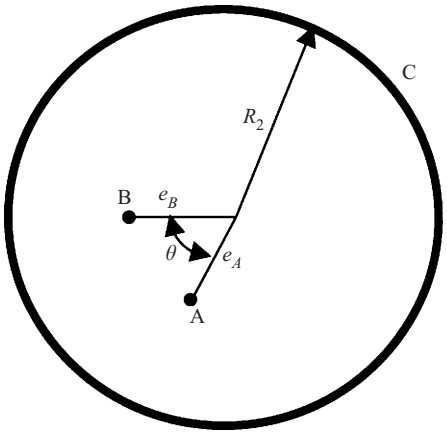

FIGURE 4. A schematic depiction of the location of the two inner electrodes A and B. e_A and e_B denote the distances of the electrodes from the cavity centre, and θ is the angle between the radii that go through the electrode locations.

predictions. Since the inner electrode is finite, the shift in the centre of rotation away from the electrode is not observed in the experiment.

2.3. *Two point electrodes*

More complicated motion than that depicted in figure 3 can be generated by utilizing two or more inner electrodes. Here we consider only two inner 'point' electrodes denoted A and B (figure 4), and we refer, as before, to the outer electrode as C.

There are many choices for possible locations of the electrodes A and B. They can be specified by their distances from the cavity centre (eccentricities), e_A and e_B, and the angle, θ, formed between the radii that pass through the electrode locations. See figure 4. In this paper, we focus only on the special cases when $e_A = e_B = 0.5$, $\theta = \pi/2$, and $\theta = \pi$. In the latter case, both electrodes are located along the same diameter of the confining cylinder C. Likewise, there is a great amount of flexibility in selecting any particular timewise variations and magnitudes of the electrode potentials.

We impose a potential difference across electrodes A and C for the time interval $0 < t < T_1$ and then a potential difference of the same magnitude (but not necessarily the same polarity) across electrodes B and C for the time interval $T_1 < t < T$. Then the process is repeated. Furthermore, we assume that the Reynolds number is small and the potential alternations are sufficiently slow so that the flow is quasi-static and the instantaneous flow field is given by the steady-state solution of the Stokes equation. This approximation is commonly used in the context of Stokes flows (i.e. Landau & Lifshitz 1959, p. 91; Aref & Balachander 1986; Chaiken *et al.* 1987).

When the potential difference is induced between electrodes A and C, we denote the resulting flow field as ψ_A. When the potential difference is induced between electrodes B and C, we denote the resulting flow field as ψ_B. Both ψ_A and ψ_B are computed using equation (18), but with two different Cartesian coordinate systems. When the potential difference alternates between AC and BC while A and B have the same polarity, the resulting flow field is

$$\psi(x, y, t) = \psi_A(x, y) f_A(t) + \psi_B(x', y') f_B(t), \tag{21}$$

provided that $f_B(t) = 0$ when $f_A(t) \neq 0$ and that $f_A(t) = 0$ when $f_B(t) \neq 0$. When

electrodes A and B are subjected to different polarities, the two electrode pairs induce motion in opposite directions; the + sign in (21) is replaced with a − sign.

One can explore various types of time-modulations (various functions $f_A(t)$ and $f_B(t)$). Here, for convenience, we select the simple protocol

$$f_A(t) = \begin{cases} 1, & kT < t < kT + T_1 \\ 0, & kT + T_1 < t < (k+1)T, \end{cases} \tag{22}$$

and

$$f_B(t) = \begin{cases} 0, & kT < t < kT + T_1 \\ 1, & kT + T_1 < t < (k+1)T. \end{cases} \tag{23}$$

In the above, $k = 0, 1, 2, \ldots$ is an integer and the resulting flow field is periodic in time with periodicity T, i.e. $\psi(x, y, t + T) = \psi(x, y, t)$. The 'on–off' nature of (22) and (23) is not quite consistent with the Stokes approximation that requires the time constant associated with the modulations to be larger than the viscous time constant. We could have easily incorporated other protocols that facilitate a smoother and more gradual transition from $f_A(t)$ to $f_B(t)$. Aref & Balachandar (1986) have, however, investigated the effects of various protocols on the kinematics of the flow between two rotating eccentric cylinders and determined that an 'on–off' protocol similar to the one specified by equations (22) and (23) gives qualitatively indistinguishable results from ones obtained with 'smoother' protocols. Indeed, functions $f_A(t)$ and $f_B(t)$ that provide a more gradual timewise change will only modify the 'effective' time interval T_i without changing the qualitative nature of the flow. Within each time interval, the passive tracer's trajectory coincides with the streamlines depicted in figure 3. Choosing a different $f(t)$ than specified in (22–23) would merely have the effect of changing the length of the segment that a particle travels along a streamline in the allotted time. In fact, we can introduce a new time variable, $\tau = \int^t f(\xi)\,\mathrm{d}\xi$, to eliminate the explicit dependence on the particular choice of $f(t)$. In the interest of minimizing the number of parameters in our problem, we chose to employ the 'on–off' protocol. Moreover, the more interesting flow phenomena occur when T is relatively large and when the quasi-static approximation is likely to be valid.

Clearly, there is a great amount of flexibility in determining the number of electrodes, their locations, and the protocols for potential magnitudes and alternations. The selection of the best parameters to achieve efficient mixing is an interesting optimization problem that we do not address here.

The motion of a passive tracer can be readily computed by numerically integrating the advection equations:

$$\dot{x} = u_x, \quad \dot{y} = u_y. \tag{24}$$

In the above, we have changed the time scale from T^* to the convective time scale R_2/U, where $U = I'BR_2/(2\pi\mu)$. The particles' trajectories were computed by integrating (24) using a fourth-order Runge–Kutta algorithm in *MatLab*.

One can imagine the trajectory that a passive tracer will follow when the electrode pairs are alternately actuated. In the time interval $kT < t < kT + T_1$, the tracer will move along a segment of the curve described by $\Psi_A = \text{const}$. In the time interval $kT + T_1 < t < (k+1)T$, the tracer will follow a segment of the curve $\Psi_B = \text{const}$. Under certain circumstances, this mechanism can lead to chaotic tracer trajectories.

The expressions for the flow field that we have obtained above are valid when only one electrode pair is active at any given time, i.e. $f_A(t)f_B(t) = 0$. Simultaneous actuation of both electrode pairs, ($f_A(t)f_B(t) \neq 0$), would alter the electric field in the cavity and render the expressions that we obtained above invalid. Nevertheless,

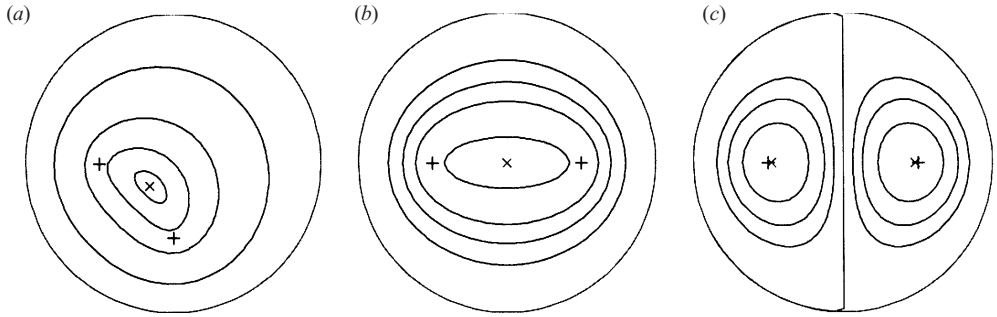

FIGURE 5. The streamlines in the limiting case of the period $T \to 0$. $e_A = e_B = 1/2$. (a) $\theta = \pi/2$ (co-rotating), (b) $\theta = \pi$ (co-rotating), and (c) $\theta = \pi$ (counter-rotating). The + and × denote, respectively, the locations of the electrodes and the stagnation points.

it is instructive to examine the flow field in the limiting case of the alternation period, $T \to 0$. This limiting case provides useful information on the flow topology. Figure 5 depicts the streamlines for a few cases when the flow fields induced by the two electrode pairs are superposed. The symbols + and × denote, respectively, the locations of the electrodes and stagnation points. In figure 5(a), $\theta = \pi/2$ and both electrodes A and B have the same polarity. The flow field consists of closed orbits that either encircle both electrodes or are confined between them. Figure 5(b) depicts the case of $\theta = \pi$ and both electrodes A and B having the same polarity. The flow field in figure 5(b) is similar to the one depicted in figure 5a. Note the presence of an elliptic stagnation point (that acts as a centre of rotation) in each of these cases. The situation is different when the electrodes A and B have different polarities (figure 5c). This arrangement necessitates changing the polarity of electrode C (we will describe in the next section how this is done in practice). In figure 5(c) one electrode pair (AC) induces clockwise motion while the other electrode pair (BC) induces counterclockwise motion. In the limit of small period T, these two motions superpose to form two families of closed orbits. One family of closed orbits has its centre of rotation (elliptic stagnation point) next to electrode A; the other family has its centre of rotation next to electrode B.

As already noted by Aref (1984) among others, equations (24) are a Hamiltonian system. The flow conserves area, and the phase space (x, y) coincides with the physical space. When $T = 0$, the system is autonomous and integrable. The phase-space portrait consists of elliptic fixed point(s) surrounded by closed orbits (tori) (figure 5). The system is analogous to a nonlinear oscillator with the period of the oscillations (τ) being dependent on the initial conditions (x_0, y_0) and ranging from zero to infinity. We refer, respectively, to orbits with rational and irrational period ratios τ/T as rational and irrational tori. Below we quote briefly a few results from dynamic systems theory.

When $T > 0$, the system may no longer be integrable. When T is small, the Kolmogorov–Arnold–Moser (KAM) theorem states that most of the orbits (the irrational tori) will distort only slightly. According to the Poincaré–Birkhoff theorem, the rational tori deform significantly and form a 'petal' structure that leads in the Poincaré section to a sequence of hyperbolic (saddle) and elliptic fixed points. The hyperbolic points give rise to chaotic behaviour while the elliptic points and the orbits surrounding them form a family of rational and irrational tori subject to the considerations enumerated above, leading to an infinite hierarchy. The net result is that, for relatively small values of T, one observes the coexistence of chaotic islands and invariant tori.

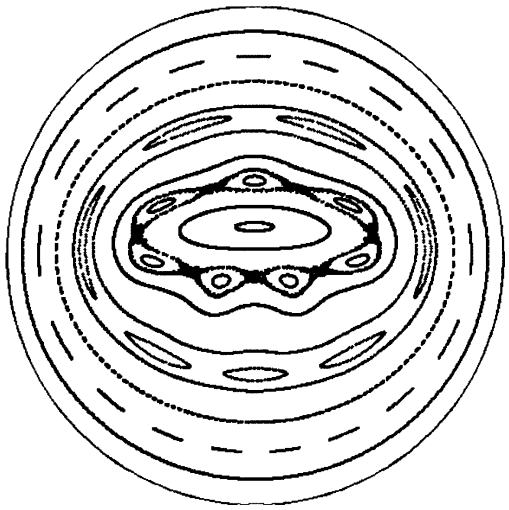

FIGURE 6. Poincaré section (stroboscopic image) when two point electrodes are positioned at $e_A = e_B = 1/2$ and $\theta = \pi$. $T_1 = T/2$, and $T = 6$. Both electrode pairs induce counter-clockwise motion.

As T increases, the chaotic areas increase in size and the regular regions shrink although they do not disappear completely. The flow topology as a function of T is described in some detail in § 4. Below, we describe briefly a few numerical experiments that illustrate the ideas described above.

Figure 6 depicts the Poincaré cross-section when $T = 6$, $T_1 = T/2$, $\theta = \pi$, and $e_A = e_B = 0.5$ for orbits with trajectories originating at $(x_0, y_0) = (1.25, 0.9)$, $(1.25, 0.8)$, $(1.25, 0.7)$, $(1.25, 0.6)$, $(1.25, 0.5)$, $(1.25, 0.4)$, $(1.25, 0.32)$, $(1.25, 0.2)$, $(1.25, 0.1)$, $(1.25, -0.45)$, $(1.25, -0.1)$. The invariant (irrational) tori trace closed orbits similar to the trajectories depicted in figure 5(b) ($T = 0$). The figure also depicts deformed rational tori. Note the appearance of hyperbolic (saddle) and elliptic fixed points. The elliptic fixed points are encircled by closed orbits that form new families of tori and that are subject to the same process as their larger counterparts. The picture is consistent with the predictions of the Poincaré–Birkhoff and KAM theorems. When T was further increased to $T = 8$, say, the Poincaré section of the trajectory starting at $(x_0, y_0) = (1.25, 0.5)$ formed a band of scattered points. When we plotted the locations of two passive tracers $\{x(t), y(t)\}$ as functions of time for two particles inserted at nearby positions (not shown here), the two trajectories followed each other closely for a short amount of time but eventually diverged widely, suggesting a positive Lyapunov exponent and a sensitivity to initial data characteristic of chaotic dynamics. Later in the paper, we calculate the correlation dimension associated with the chaotic motion and show that its magnitude is consistent with chaotic behaviour. In summary, the chain of events as T increases is very similar to what has been observed in many chaotic Hamiltonian systems (see, for example, Ottino 1989, pp. 143–152).

3. Flow visualization experiments

Along with the numerical computations, we also carried out a few crude, qualitative experiments. The objective of the experiments was to illustrate that similar flows to the ones predicted here can be also observed in practice. The experimental apparatus is similar to that depicted in figure 1. To facilitate easy introduction of dye in the experiments, the stirrer's cavity was not capped. The stirrer's circumference was made

of a metal washer with a radius $R_2 = 7.8\,\text{mm}$ and a height of 2 mm. The inner electrodes A and B were made out of copper wires of radii $R_1 = 0.35\,\text{mm}$. Since $R_1 \ll R_2$, the theory that treats the inner electrodes as points should provide a reasonable description of the flow field. Earlier attempts at printing the electrodes with metal inks were frustrated by the relatively rapid consumption of the electrodes. In all our experiments, $e_A = e_B = R_2/2$. The working fluid was ~ 0.1 M saline solution. When the voltage drop across the electrodes was below a certain threshold of about $V_0 \sim 2\,\text{V}$, little current passed in the solution. For example, when $V = 0.25\,\text{V}$, the apparent specific conductivity $\sigma \sim 5 \times 10^{-3}\,\Omega^{-1}\,\text{m}^{-1}$. As the potential difference increased, the apparent specific conductivity increased, achieving a value of about $0.06\,\Omega^{-1}\,\text{m}^{-1}$ at the potential difference of 1 V. Apparently, below the threshold V_0, the electrodes are impervious to Na^+ ions (Levich 1962), and the current is carried by various impurities in the solution. At potential differences well above 2 V, the specific conductivity was nearly constant at about $1\,\Omega^{-1}\,\text{m}^{-1}$. Our experiments were carried out for potential differences ranging from 0.3 to 7 V.

A neodymium (NdFeB) permanent magnet of approximate intensity $B = 0.3\,\text{T}$ (Edmund Scientific CR81-23) provided the magnetic field. The magnetic field's intensity was measured with a gauss meter. The electrodes were connected via computer-controlled relay actuators and a D/I card (PCL-725, Advantech Co., Ltd.) to the terminals of two DC-power supplies (Hewlett Packard, HP 6032A). The relays were programmed to switch 'on' and 'off' in such a way that only one electrode pair (either AC or BC) was active at any given time. In other words, when $kT^* < t < kT^* + T_1^*$ ($T_1^* > 0$), the pair AC was activated while the pair BC was disconnected from the power supply. When $kT^* + T_1^* < t < (k+1)T^*$, the pair BC was activated while the pair AC was disconnected. The superscript * denotes dimesional quantities. In our experiments, T^* ranged from 2 to 4 s and $T_1 = T/2$. T^* was chosen to be relatively small to avoid significant effects of dye diffusion and migration in the electric field. In one arrangement, the electrodes A and B were both connected to the power supply's plus terminal while C was connected to the minus terminal. This resulted in both electrode pairs inducing circulation in the counterclockwise direction. In a second arrangement, during the first part of the period, A and C were connected, respectively, to the plus and minus terminals while in the second part of the period, C and B were connected, respectively, to the plus and minus terminals. In other words, C's polarity changed at mid-period. This arrangement induced counterclockwise circulation in the first half of the period and clockwise circulation in the second half of the period. We varied the effective (dimensionless) period, T, by varying the potential difference across the electrodes, that in turn, affected the system's characteristic time and the actual (dimensional) period T^*.

The flow field was visualized by introducing a drop of dye at various locations inside the cavity. The dye consisted of a solution of Blue Dextran (SIGMA Chemical Co.) in Fluorescent Liquid Dye (Cole-Parmer Instrument Company). Although the two dyes had vastly different diffusion coefficients, we used a mixture of dyes rather than a single one because the individual dyes appeared to be charged and tended to drift in the electric field. This drift was much reduced when the mixture of the two dyes was used. The flow visualization allowed us to obtain only a crude qualitative description of the flow field. The images of the flow field were captured with both video and still cameras. The movies provide a much more vivid account of the evolution of the dye tracers.†

† A sample video clip is available at http://www.seas.upenn.edu/~bau/Movie 2 Ecc.avi

In our experiments, we did not observe any significant bubble generation. This is consistent with the low electrical currents transmitted through the apparatus. Over time, however, the electrodes degraded. This could be a problem in a practical device designed to operate for an extended period of time. The erosion problem can be significantly reduced or even eliminated by appropriate selection of electrode material and/or through the use of an AC electric and magnetic fields. By appropriate synchronization of the electromagnetic field with the AC current, the diretion of the Lorentz force would remain unaltered (i.e. Lemoff & Lee 2000).

Clearly, there are many differences between the two-dimensional model presented earlier in the paper and the experimental set-up described in this section. Although one can model the time-dependent three-dimensional flow in the apparatus, such a model will be too cumbersome and of little use for studying the evolution of the chaotic advection. For the study of the trajectories of a passive tracer over very many periods, one needs relatively simple and highly accurate expressions for the velocity field. Therefore, when studying chaotic stirring, many researchers have invoked a two-dimensional quasi-static approximation. To illustrate that our model retains the essential physics of the stirring process, we compare in the Appendix the two-dimensional quasi-static flow with a Hele-Shaw model and with a time-dependent model. Based on these comparisons, it appears that similar physical mechanisms are at work in both the experiments and the theory.

4. Results and discussion

We activated the two electrode pairs according to the protocol detailed in (22) and (23). In some of the figures below, we show stroboscopic images. These images were obtained by integrating equation (24), which describes the motion of a passive tracer, and documenting the tracer's location at the end of each period. In other words, each image is a superposition of snapshots that depict the location of the tracer particle at times $t = kT$, where $k = 0, 1, 2, \ldots$. Such stroboscopic images are referred to as Poincaré sections and they are often used as a diagnostic tool to determine the effectiveness of the stirring process. When the pattern of points that emerges lies on a smooth curve, the motion is deemed to be regular (poor stirring). A scattered pattern corresponds to chaotic motion. All the results presented in this section correspond to $e_A = e_B = R_2/2$ and $T_1 = T/2$. The corresponding bi-cylindrical coordinates are $\alpha_1 = \infty$, $\alpha_2 = \log(2)$ and $a = 0.75$.

Figure 7 depicts the Poincaré sections for various periods $T = 4$ (*a*), 8 (*b*), 20 (*c*) and 50 (*d*) when $\theta = \pi/2$ and both electrode pairs induce counterclockwise motion. Note the different advection patterns that evolve as the period T increases. Figure 7(*a*) depicts trajectories of particles initially positioned at locations $(x, y) = (1.25, 0)$, (1.45, 0.2), (1.65, 0.4) and (1.85, 0.6). The passive tracer's trajectory is only slightly jittery as it is alternately influenced by the flow fields induced by the two pairs of electrodes. Since the period is relatively small, the tracer does not have sufficient time to stray away from its mean, regular path. The net result is that the stroboscopic image (figure 7*a*) appears regular, depicting closed orbits that either encircle electrodes A and B or are confined between them. The flow topology is very similar to the one corresponding to the limiting case of $T = 0$ (figure 5*a*). In most of the domain, the tracer's orbits appear to remain closed and regular until T exceeds ~ 4.4.

As the period T increases, the tracer strays a larger distance away from its 'regular path', leading to a more complicated motion. When $T = 8$, figure 7(*b*) depicts particle trajectories with initial positions $(x, y) = (1.05, -0.2)$, $(1.25, 0)$, $(1.5, 0.25)$ and

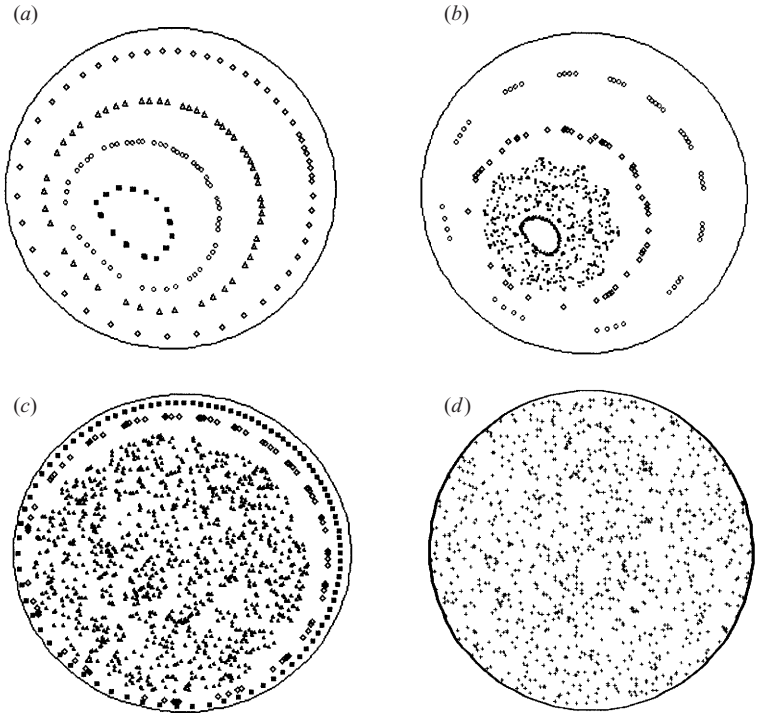

FIGURE 7. Poincaré sections (stroboscopic images) when two point electrodes are positioned at $e_A = e_B = 1/2$ and $\theta = 90°$. $T_1 = T/2$. Both electrode pairs induce counter-clockwise motion. (*a*) $T = 4$, (*b*) $T = 8$, (*c*) $T = 20$, and (*d*) $T = 50$.

(1.75, 0.5). An irregular region or chaotic island is visible between the inner and outer regular regions. As the period T is further increased, the chaotic region spreads to cover most of the cavity and wipes out the regular core. When $T = 20$, figure 7(*c*) depicts trajectories of particles inserted at $(x, y) = (1.9, 0.65)$, (1.8, 0.55) and (1.25, 0). Only a thin regular layer is visible in the vicinity of the outer cylinder's surface. A further increase in T leads to a further spreading of the irregular region. When $T = 50$, figure 7(*d*) depicts the trajectory of a single particle inserted at location $(x, y) = (1.25, 0)$. The chaotic region appears to cover the entire cavity. Figure 7 illustrates the disintegration of regular trajectories as the period T increases. Although the underlining flow field is quite simple, the advection patterns are complex.

Next, we examined the case of $\theta = \pi$ and both electrode pairs inducing motion in the same sense (counterclockwise). Figure 8(*a*, *b*, *c*) (left column) depicts respectively, the Poincaré sections when $T = 4$, 10 and 40. We also include photographs of flow visualization experiments (right column). Keep in mind, however, that the photographs represent actual dye trajectories and not stroboscopic images. Furthermore, due to the smallness of the apparatus, diffusion (which is ignored in the mathematical model) played a significant role in the experiment. When $T = 4$, figure 8(*a*) depicts the trajectories of particles with initial positions $(x, y) = (0.4, 0)$, (0.55, 0), (0.7, 0), (0.85, 0) and (1,0). In most of the section, the motion appears to be regular. The Poincaré section features closed trajectories that either encircle both electrodes A and B or are confined between these two electrodes. The flow visualization photograph exhibits similar behaviour. The spread of the dye is partially due to diffusion and partially due to the jittery motion caused by the trace particles being alternately captured

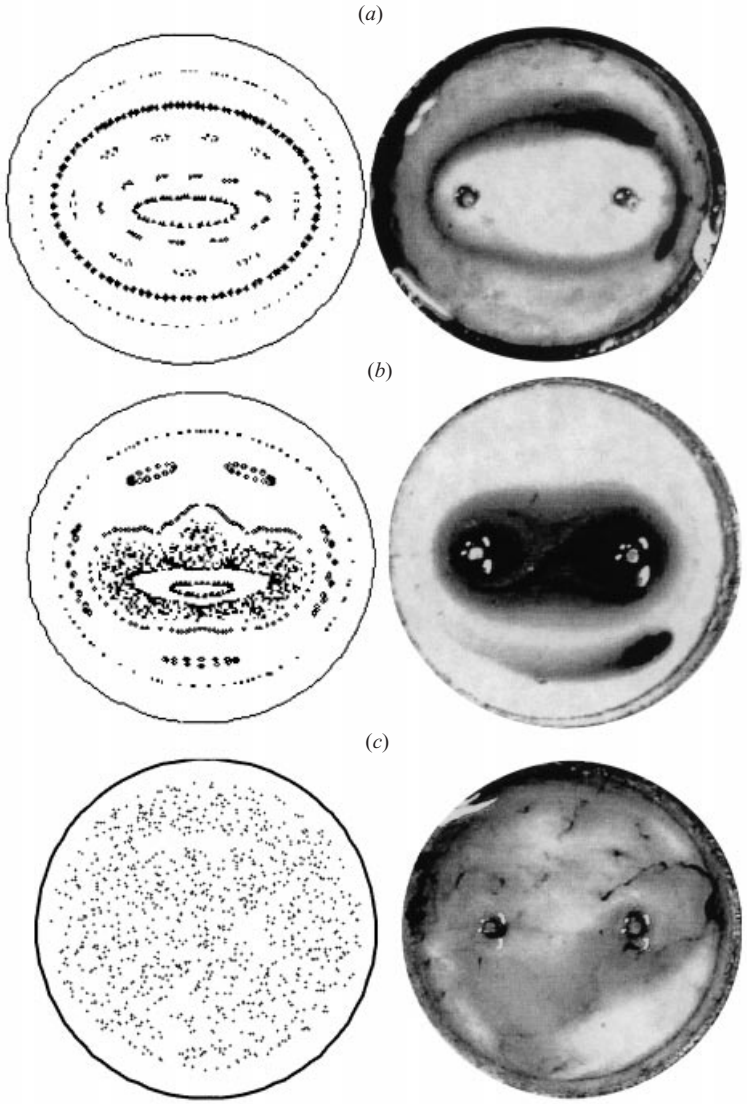

FIGURE 8. Poincaré sections (stroboscopic images, left column) and flow visualization photographs (right column) when $e_A = e_B = 1/2$ and $\theta = \pi$ (co-rotating). $T_1 = T/2$. (*a*) $T = 4$, (*b*) $T = 10$, and (*c*) $T = 40$.

by the velocity fields induced by each electrode pair. When $T = 10$, figure 8(*b*) depicts the trajectories of particles inserted at $(x, y) = (0.4, 0)$, (0.5, 0), (0.6, 0) (0.7, 0) and (1.25, −0.1). A chaotic island is visible between the inner and outer regular regions. Unfortunately, we were not able to duplicate in the experiment all the features of the numerical simulation. Nevertheless, the dye traces exhibit a chaotic core and outer regular region, and the rapid spread of the dye (which is much more vividly captured in the movie) in the region next to electrodes A and B provides partial evidence of the existence of a chaotic island. As T increases further, the chaotic region spreads and the regular regions shrink. When $T = 40$, figure 8(*c*) depicts the trajectory of a single particle inserted at $(x, y) = (1.25, 0)$. The chaotic region appears to have spread

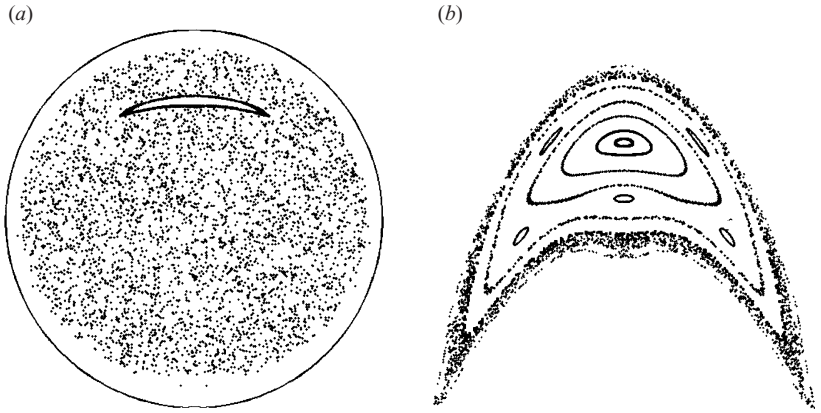

FIGURE 9. Poincaré section (stroboscopic image) depicting an island of regularity (a) and enlargement of the regular region (b) when $e_A = e_B = 1/2$ and $\theta = \pi$ (co-rotating) and $T = 60$.

to wipe out the regular regions completely. Flow visualization experiments conducted at relatively large T exhibit a rapid spread of the dye to cover the entire region.

The chaotic regions depicted in figure 8 contain islands of regular behaviour. An example of such an island of regularity is depicted in figure 9(a) when $T = 60$. Figure 9(b) zooms in on the regular region to reveal finer structures that consist of invariant tori and perhaps chaotic subregions. As T increases, the regular region shrinks and moves upward.

In order to characterize the chaotic behaviour, we computed the correlation dimension $D(1 \leqslant D < 2)$ (Grassberger & Procaccia 1983). Briefly,

$$C(r) = \left(\frac{n}{2}\right)^{-1} \sum_{i=1}^{n-1} \sum_{j=i+1}^{n} H(r - \|\boldsymbol{x}_i - \boldsymbol{x}_j\|) \tag{25}$$

is the probability that two arbitrary points, $\boldsymbol{x}_i$ and $\boldsymbol{x}_j$, on a tracer's orbit are closer together than distance r. $H(u) = 1$ when $u > 0$ and $H(u) = 0$ when $u \leqslant 0$; $\|.\|$ denotes a norm in two-dimensional Euclidean space, i.e. $\|\boldsymbol{x}_i - \boldsymbol{x}_j\| = \sqrt{(x_i - x_j)^2 + (y_i - y_j)^2}$. For sufficiently small r, one expects that $C(r) = ar^D$, and the correlation dimension is defined as

$$D = \frac{\mathrm{d}\log C(r)}{\mathrm{d}\log r}. \tag{26}$$

We verified our code by calculating the correlation dimension for the Henon map and obtaining an excellent agreement (within 0.3%) with published data. Figure 10 depicts the correlation dimension D as a function of the period T for the conditions of figure 8; 15 000 points were used in the calculation of D. This was deemed to be sufficient since changes in the number of points from 11 000 to 15 000 in increments of 1000 ($T = 80$) led to variations in D smaller than 0.5%. When $T < 4$, $D \sim 1$ which indicates that in most of the cross-section the motion is regular. When $T > 4$, the correlation dimension increases and assumes a value of $D \sim 1.9$ when $T \sim 80$. $D > 1$ is consistent with chaotic flow. D does not appear, however, to be a useful measure for the stirrer's effectiveness.

Next, we examine the effect of the direction of rotation on the evolution of chaotic advection. In figure 11, we examine the case when the two electrodes are positioned at an angle $\theta = \pi$ apart and when one electrode pair AC (say) induces counterclockwise

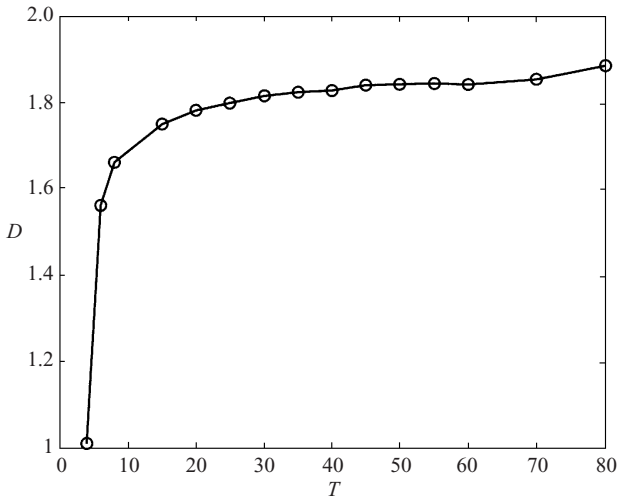

FIGURE 10. The correlation dimension D is depicted as a function of the period T when $e_A = e_B = 1/2$ and $\theta = \pi$ (co-rotating).

motion and the other electrode pair, BC, induces clockwise motion. The top (I), middle (II), and bottom (III) rows in figure 11 depict, respectively, Poincaré sections, the actual trajectories of the passive tracer, and photographs of flow visualization experiments. The columns (a), (b) and (c) correspond, respectively, to $T = 2$, 6 and 8. When $T = 2$ (figure 11 Ia), the motion depicted in the Poincaré section is mostly regular and consists of two sets of closed orbits, one set encircling electrode A and the other set encircling electrode B. The tracers were introduced at locations $(x, y) = (0.26, 0)$, (0.4, 0), (0.5, 0), (1.45, 0), (2.0), (2.1, 0) and (2.24, 0). Figure 11-IIa depicts the actual motion of the tracer. Witness the presence of jitters resulting from the tracer being trapped (at different times) by the flow fields induced by the two electrode pairs. The presence of two families of periodic orbits is well supported by the flow visualization experiments (figure 11 IIIa). As the period T increases (i.e. $T = 6$), chaotic islands become visible. In figure 11(Ib) the passive tracers were introduced at locations $(x, y) = (0.3)$, (0.5, 0), (0.8, 0), (1.1, 0), (1.5, 0), (1.55, 0) and (1.75, 0). Figure 11-IIb illustrates that as the period increases, so does the magnitude of the jitters. The presence of the global structure consisting of two counter-rotating circulations is visible in figure 11-IIIb. When $T = 8$, figure 11(Ic) depicts the trajectory of a single tracer inserted at $(x, y) = (1.25, 0)$. The irregular chaotic region appears to have spread to cover almost the entire cavity. Similar to figure 11(Ic) the flow visualization experiments (figure 11 IIIc) illustrate the presence of counter-rotating eddies through the existence of an unmixed zone at the ends of the diagonal that is perpendicular to the line connecting electrodes A and B (figure 11 IIIc).

To examine the effect of the stirrer in enhancing mixing, like Aref (1984), we tracked the deformation of a material blob (figures 12 and 13). To this end, we inserted a square material blob of edge size 0.15, initially centred at (1.125, 0.375), and tracked its evolution as a function of time for various stirring periods. Figures 12 and 13 depict, respectively, the evolution of the blob when the electrode pairs are inducing co-rotating and counter-rotating circulation. In both cases, $\theta = \pi$ and $e_A = e_B = 0.5$. Figures 12 and 13 should be cross-referenced, respectively, with figures 8 and 11. The

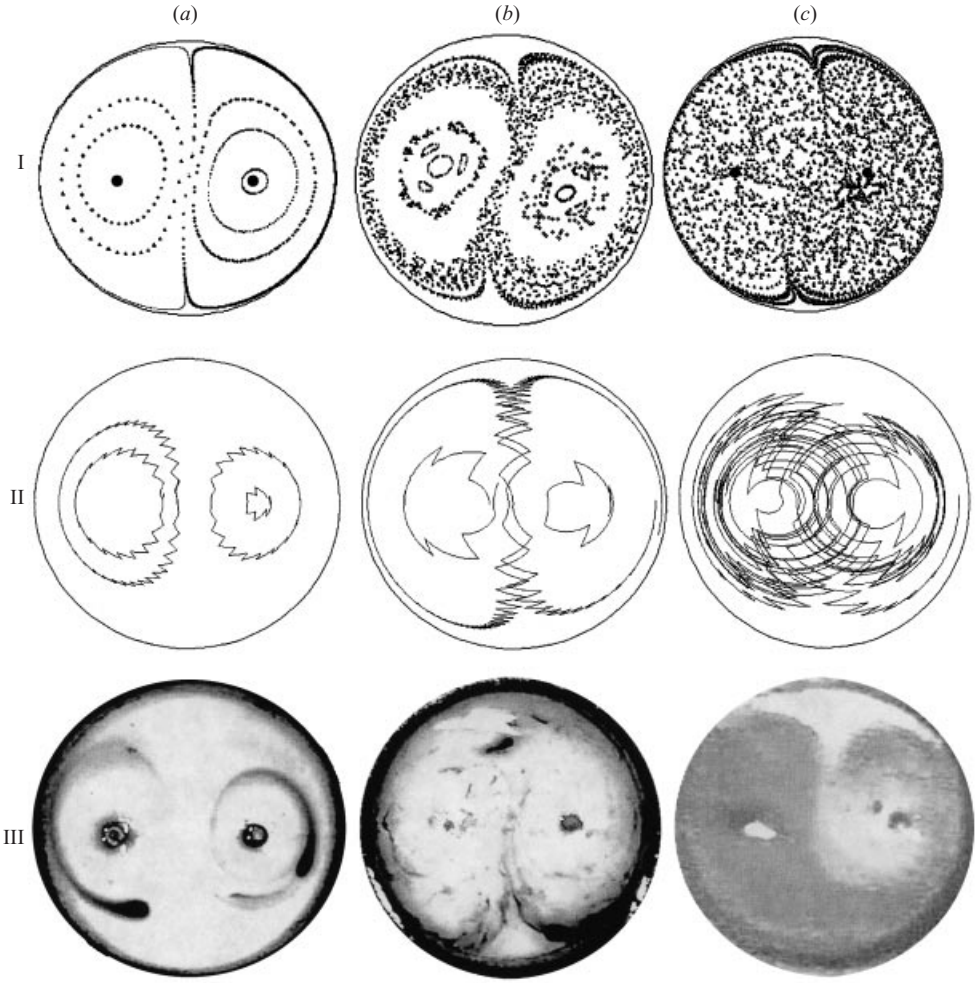

FIGURE 11. Poincaré sections (stroboscopic images, row I), actual passive tracers' trajectories (row II), and flow visualization photos (row III) when $e_A = e_B = 1/2$, $\theta = \pi$ (counter-rotating), and $T_1 = T/2$. (*a*) $T = 2$, (*b*) $T = 6$, and (*c*) $T = 8$.

evolution of the blob was tracked by integrating the trajectories of 10^4 points initially evenly distributed within the square.

When $T = 4$, figure 12(*a*) depicts the initially square blob at times $t = 0$, $T, 2T, \ldots, 8T$. When the period is relatively small, the blob stretches, deforms and elongates slowly. It is confined essentially to a closed orbit that encloses both internal electrodes. At this period, the flow, as depicted in the Poincaré section (see figure 8*a*), appears regular. The process accelerates as the period increases. When $T = 10$, figure 12(*b*) depicts the blob at times $t = 0, T, 2T, 3T$ (figure 12*b*1), and $4T, \ldots, 7T$ (figure 12*b*2). Note that at $t \sim 5T$, the blob turns into a thin strip and it starts folding upon itself; it is still confined to a relatively narrow band that encircles both internal electrodes. Although the particles have been stirred, they occupy only a small region of the cavity. When $T = 20$, figure 12(*c*) depicts the blob at $t = 0, T$ (figure 12*c*1), $2T$, $3T$ (figure 12*c*2), $4T$ (figure 12*c*3), $5T$ (figure 12*c*4), $8T$ (figure 12*c*5), and $10T$ (figure 12*c*6). Here, after one period (figure 12*c*1), the square blob has already turned

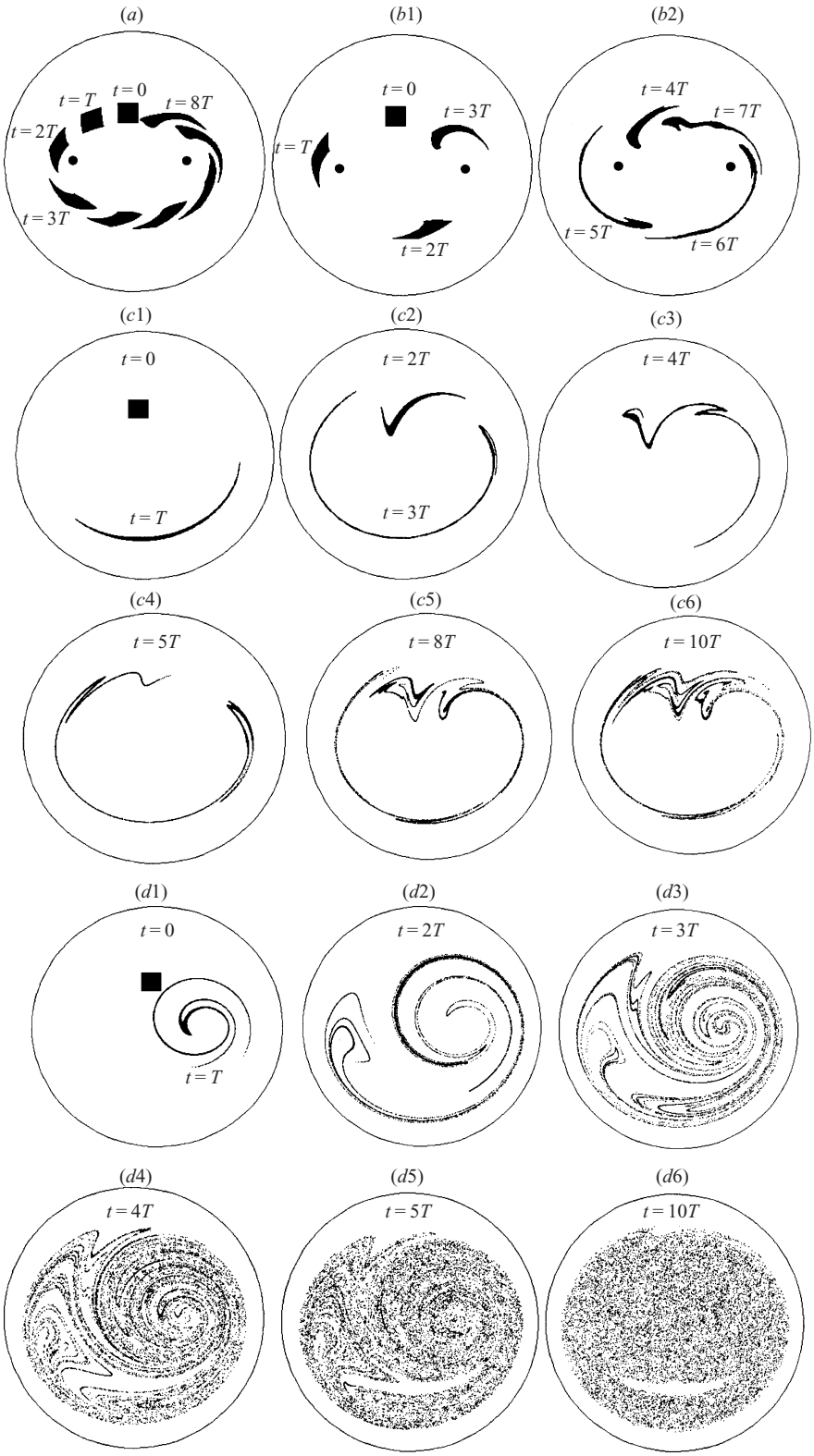

FIGURE 12. The deformation of a material blob of edge size 0.15 initially ($t = 0$) centred at (1.125, 0.375) at various times $t = kT$ and various periods (*a*) $T = 4$, (*b*) $T = 10$, (*c*) $T = 20$, and (*d*) $T = 40$. $e_A = e_B = 1/2$, $\theta = \pi$ (co-rotating), and $T_1 = T/2$.

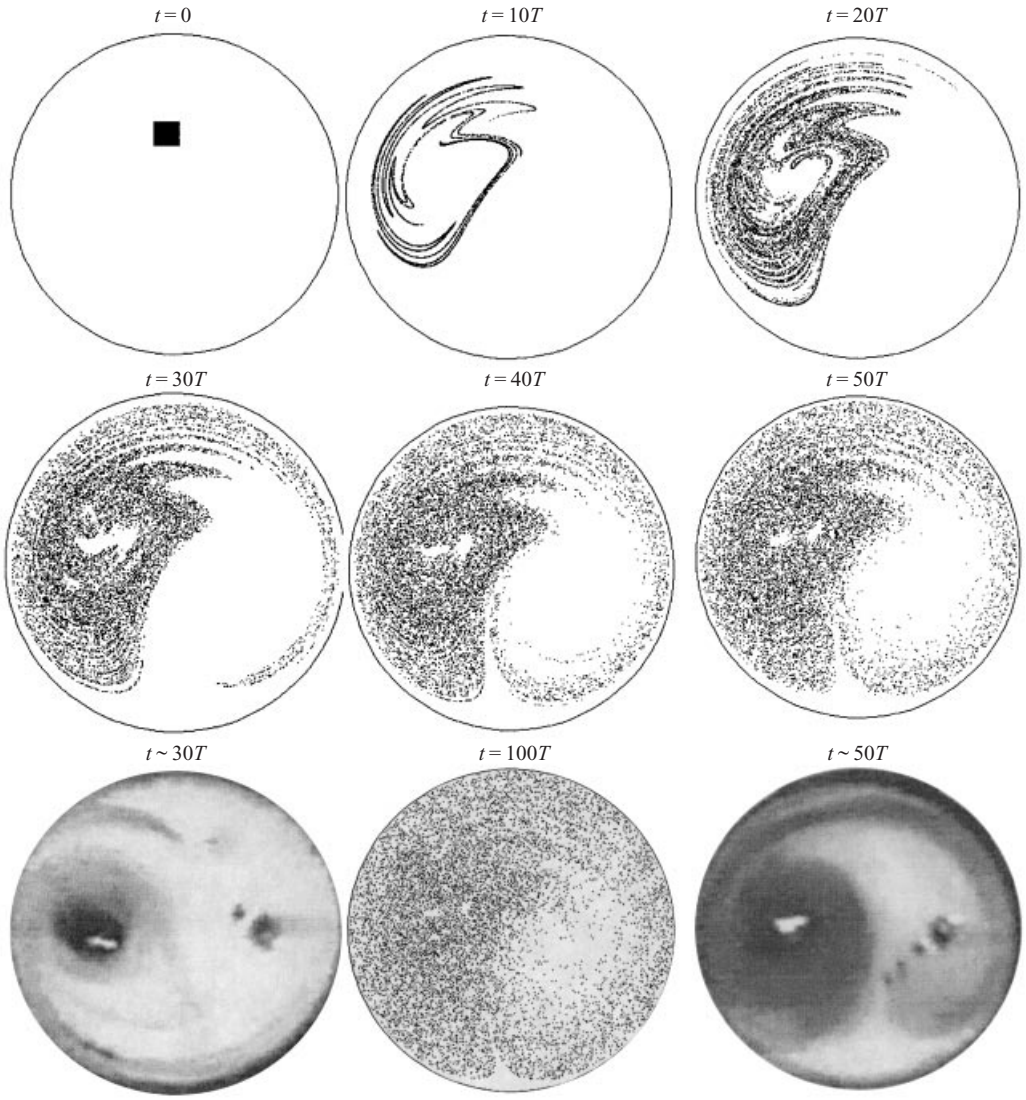

FIGURE 13. The deformation of a material blob of edge size 0.15 initially ($t = 0$) centred at (1.125, 0.375) at various times $t = kT$. $e_A = e_B = 1/2$, $\theta = \pi$ (counter-rotating), $T = 8, T_1 = T/2$, and various times $t = 0$, $10T$, $20T$, $30T$, $40T$, $50T$, and $100T$. Also shown are two flow visualization photographs at estimated times $t \sim 30T$ and $50T$.

into a thin line. Subsequent images illustrate the line's folding. The locally complicated behaviour exhibited in figure 12c6 is consistent with the presence of a chaotic island (figure 8b). When $T = 40$, figure 12(d) depicts the blob at times $t = 0$, T (figure 12d1), $2T$ (figure 12d2), $3T$ (figure 12d3), $4T$ (figure 12d4), $5T$ (figure 12d5), and $10T$ (figure 12d6). The figures illustrate the stretching and folding process that is consistent with the nearly 'global' chaos depicted in figure 8(c). In other words, the fluid particles spread to cover almost the entire cavity area. Despite the fact that our process is viscous while the one described by Aref (1984) is inviscid, figure 12(d) shares many similarities with Aref's (1984) figure 6. Figure 12(d) also illustrates the

presence of exclusion zones, one next to the cavity's circumference and the other shaped like a 'mouth' in the lower half of the cavity (figure 12*d* 6).

When $T = 8$, figure 13 depicts the blob's evolution when the two vortices are counter-rotating at times $t = 0$, $10T$, $20T$, $30T$, $40T$, $50T$ and $100T$. At about $t \sim 100T$, the fluid particles wander to cover almost the entire cavity area. The process is quite similar to the one that we observed in flow visualization experiments. We also include in figure 13 two photographs that somewhat resemble the structures observed at $t \sim 30T$ and $50T$. Of course, the conditions used in the computations (a square blob) and in the experiment (a blob of ill-defined shape) are vastly different. Nevertheless, it is interesting to observe qualitative similarities between the theoretical predictions and the experimental observations.

5. Conclusions

The paper provides a practical example of a time-periodic, low-Reynolds-number flow that exhibits chaotic behaviour. The theoretical predictions are in good qualitative agreement with experimental observations. We have demonstrated that two alternating 'agitators' can induce complicated motions and that the complexity of the motion increases as the period of alternation increases. We chose a circular geometry because of the availability of relatively simple analytic solutions to the Stokes problem. Similar ideas can, of course, be implemented in other geometries such as a rectangular confining chamber or a flow-through conduit. Moreover, the stirrer does not require rigid walls. Indeed, the stirrer's geometry is dictated by the deposition of the peripheral electrode C. Since the electrode can be either printed or photolithographically patterned, one can produce fairly complicated shapes. Furthermore, one can employ a larger number of agitators than the two that we have used here and more complicated protocols of timewise variations. An interesting optimization problem is the selection of the peripheral electrode's geometry, the location and number of agitators, and a timewise alternation protocol to induce the most efficient stirring. The motion in our device is induced through magnetohydrodynamic forces; thus, the stirrer does not require any moving parts. Variations of the device employed in our study can be fabricated on a much smaller scale to provide stirring in microfluidic systems. Some potential disadvantages of the MHD stirrer are electrode erosion, significant bubble generation when the current intensity increases, and the possible migration of charged particles and molecules in the electric field. Many of these disadvantages can be alleviated through the use of alternating, synchronized electric and magnetic fields.

The work described in this paper was supported, in part, by DARPA (Dr Anantha Krishnan, Program Director) through a grant to the University of Pennsylvania. Dr Jianzhong Zhu assisted in constructing the experimental set-up.

Appendix

In order to study the chaotic advection, we used a relatively simple description of the flow field. Although there are many differences between the experimental apparatus and the theoretical model, the same physical mechanisms are at work in both the theoretical model and the experiment. In this Appendix, we examine briefly some of the differences between the actual flow in the experimental apparatus and the two-dimensional quasi-static model. The Appendix consists of two parts: in the first,

we compute the flow field in a shallow cavity using the Hele-Shaw approximation; in the second, we examine the quasi-static approximation. The computations were carried out with the aid of the finite element package FemLab† version 2.1. To facilitate a numerical solution, we carried out the computation for an inner electrode of dimensionless radius 0.25 confined in a cavity of radius 1. The eccentricity is 0.5. The two-dimensional time-independent finite-element calculations were compared with and found to be indistinguishable from the analytic solution (equation(8)).

Since the experimental apparatus consists of a shallow cylinder, it is appropriate to simulate the flow in the experimental apparatus using the Hele-Shaw (H-S) approximation. We denote, respectively, the dimensionless and dimensional heights of the apparatus as $2H$ and $2H^*$ ($H = H^*/R_2$). Furthermore, we assume that the velocity distribution is parabolic (in z) and that the pressure is uniform in the vertical ($-H \leqslant z \leqslant H$) direction (see, for example, Yih 1979, p. 382). Accordingly, the two-dimensional velocity vector $\boldsymbol{u} = u_x\hat{\boldsymbol{e}}_x + u_y\hat{\boldsymbol{e}}_y = \frac{3}{2}(1-z^2/H^2)\hat{\boldsymbol{u}}(x, y)$ satisfies the non-slip boundary condition at $|z| = H$. $\hat{\boldsymbol{u}}(x, y)$ is the average velocity along the cavity's height, and it satisfies the two-dimensional continuity equation $\nabla \cdot \hat{\boldsymbol{u}} = 0$. The momentum equation (Brinkman 1947) is

$$St^2\frac{\partial \hat{\boldsymbol{u}}}{\partial t} = -\nabla V \times \hat{\boldsymbol{e}}_z - \nabla p + \nabla^2\hat{\boldsymbol{u}} - \frac{3}{H^2}\hat{\boldsymbol{u}}. \tag{A 1}$$

In the above, we removed the factor $(\alpha_1 - \alpha_2)$ from the velocity scale (3), and $\nabla = \hat{\boldsymbol{e}}_x\partial/\partial x + \hat{\boldsymbol{e}}_y\partial/\partial y$ is a two-dimensional operator.

In the main body of the paper, we solved the time-independent version of (A1) in the limit $H \to \infty$. In the other extreme of $H \to 0$, we can drop the term $\nabla^2\hat{\boldsymbol{u}}$, and the time-independent version of (A1) assumes the form of Darcy's equation,

$$0 = -\nabla V \times \hat{\boldsymbol{e}}_z - \nabla p - \frac{3}{H^2}\hat{\boldsymbol{u}}. \tag{A 2}$$

Since equation (A2) is of a lower order than equation (A1), it cannot satisfy the non-slip condition at the cylindrical boundaries. Formally, the domain can be divided into a core region where $\nabla^2\hat{\boldsymbol{u}}$ is negligible (to $O(H^2)$) and boundary layer regions in which $\nabla^2\hat{\boldsymbol{u}} \sim H^{-2}\hat{\boldsymbol{u}}$. The advantage of (A1) is that it includes the boundary-layer structure and provides predictions that are in better agreement with experimental observations than (A2) (i.e. Fernandez *et al.* 2002). Equation (A2) can, however, be readily solved in a closed-form. Below, we provide an analytical solution for (A2) and a numerical solution for (A1).

The solution of (A2) proceeds along similar lines to the process described in § 2.1. Briefly, we use the bi-cylindrical coordinate system and introduce the stream function (Ψ). The streamfunction satisfied the Laplace equation $\nabla^2\Psi = 0$ with the boundary conditions $\Psi(\alpha_1, \beta) = 0$ and $\Psi(\alpha_2, \beta) = W$, where the constant W is determined by requiring the pressure to be a unique function of β. The appropriate solution is

$$\Psi = \left(-\frac{H^2}{3}\right)\frac{\alpha_1 - \alpha}{\alpha_1 - \alpha_2} \tag{A 3}$$

The flow field consists of closed contours similar to the ones depicted in figure 15. By periodically alternating the flow field, one would observe chaotic behaviour of a similar nature to what we described in § 4.

Since the full equation (A1) is not separable in bi-cylindrical coordinates, we can either construct a series solution or resort to numerical techniques. We chose the latter.

† FEMLAB is a product of COMSOLAB, Tengnergatan 23, SE-111 40 Stockholm, Sweden.

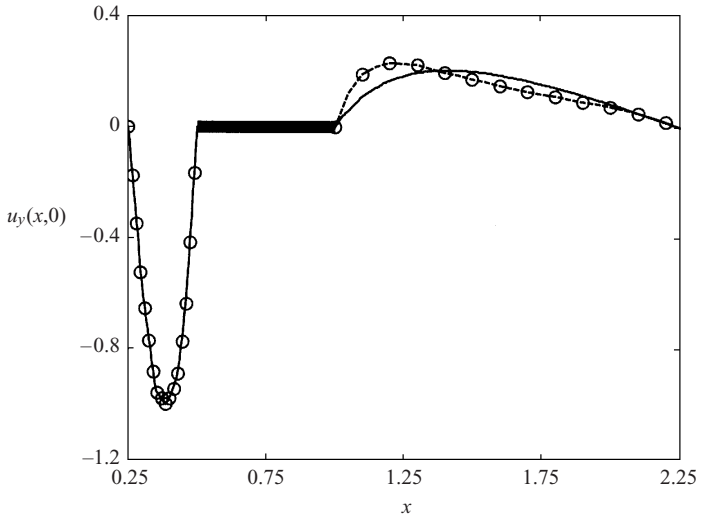

FIGURE 14. Comparison between Hele-Shaw (dashed line and circles) and two-dimensional (solid line) time-independent flows. The velocity $u_y(x,0)$, normalized with its maximal value, is depicted as a function of x. $R_1/R_2 = 0.25$, $R_2/H^* = 4$, and $e_c = 0.5$.

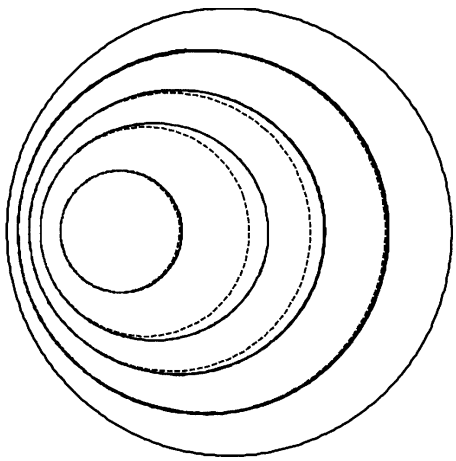

FIGURE 15. The streamlines of the Hele-Shaw flow (dashed lines) are compared with the two-dimensional streamlines (solid line). $R_1/R_2 = 0.25$, $R_2/H^* = 4$, and $e_c = 0.5$.

We use $(R_2/H^*) = 4$, which is roughly comparable to the situation in our experiment (free top surface). When $St = 0$, $R_1/R_2 = 0.25$ and $e_c = 0.5$, figures 14 and 15 depict, respectively, the normalized velocity $u_y(x,0)/\mathrm{Max}_x(u_y(x,0))$ as a function of x and the streamlines for the two-dimensional (solid line) and the H-S (dashed line) flows. In figure 14, we also use hollow circles to help distinguish the H-S flow from the two-dimensional profile. In figure 14, $\mathrm{Max}_x(u_y^{HS}(x,0))/\mathrm{Max}_x(u_y^{2D}(x,0)) \sim 0.6$. Although the two flow fields are not identical in detail, they are qualitatively quite similar, and it is reasonable to expect that the H-S model will exhibit chaotic advection similar to what we observed in the two-dimensional simulations.

Next, we compare the quasi-static flow field with an actual time-dependent flow field in the Hele-Shaw cell. The quasi-static approximation assumes that the velocity

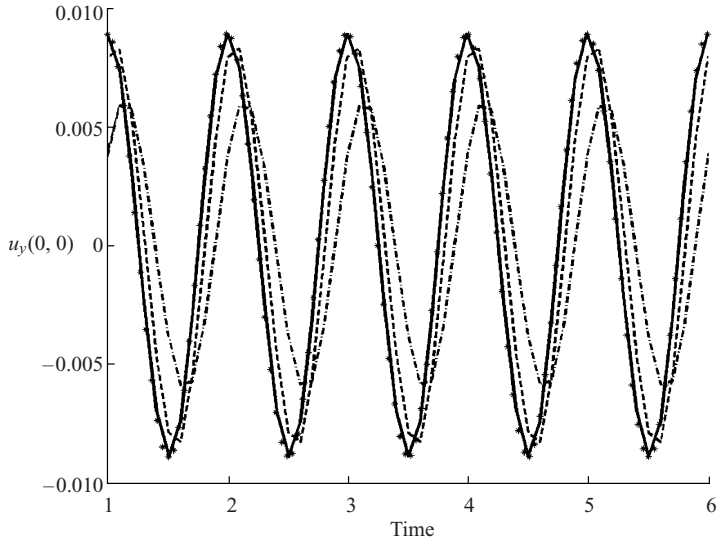

FIGURE 16. Comparison between the quasi-static approximation (solid line) and the time-dependent flows with $St^2 = 1(*)$, $St^2 = 9$ (dashed line), and $St^2 = 25$ (dashed-dot line). $u_y(0,0)$ is depicted as a function of time. $R_1/R_2 = 0.25$ and $e_c = 0.5$.

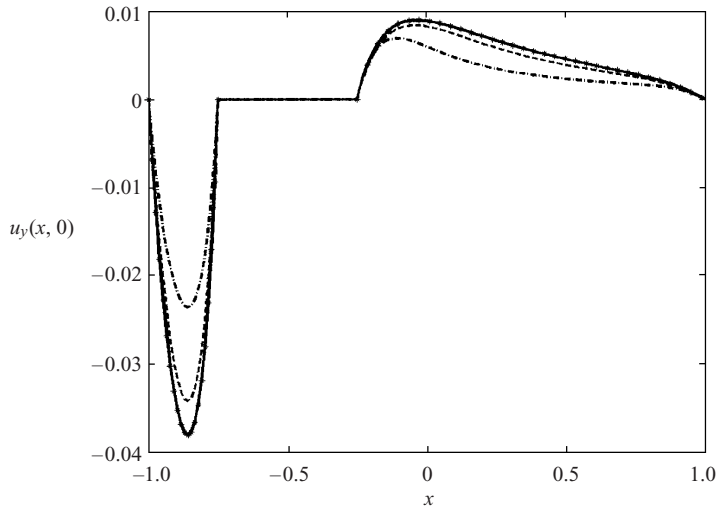

FIGURE 17. The instantaneous $u_y(x,0,t_1)$ quasi-static approximation (solid-line) and the time-dependent velocity profiles $St^2 = 1(*), St^2 = 9$ (dashed line), and $St^2 = 25$ (dashed-dot line) are depicted as a function of x. $R_1/R_2 = 0.25$ and $e_c = 0.5$.

$\boldsymbol{u}(x,y,t) \sim \boldsymbol{u}_s(x,y)F(t)$, where $F(t)$ is the protocol used to alter the voltage and $\boldsymbol{u}_s(x,y)$ is the time-independent flow field. Here, we use $F(t) = \cos(2\pi t)$. We integrated numerically equation (A1). Once initial transients died out figures 16 and 17 depict, respectively, the velocity $u_y(0,0,t)$ as a function of time and the instantaneous velocity distribution $u_y(x,0,t_1)$ as a function of x when the quasi-static approximation is invoked (solid line), when $St^2 = 1(*)$, $St^2 = 9$ (dashed line), and $St^2 = 25$ (dashed-dot line). The time t_1 in figure 17 was chosen to coincide with the point of maximum amplitude in figure 16. On the scale of the figures, when $St^2 = 1$, the time-dependent

flow field is essentially indistinguishable from the quasi-static approximation. When $St^2 = 9$, the time-dependent flow exhibits a time-lag and slightly reduced amplitude in comparison with the quasi-static flow. This relatively good agreement is partially due to the fact that in the H-S cell, the effective Stanton number ($3^{-1/2}HSt$) is significantly smaller than St. As the frequency of the oscillations and St increase, the amplitude of the oscillations decreases and the time-lag increases.

Based on the analysis in this Appendix, it is reasonable to assume that similar stirring mechanisms are at work in the two-dimensional model and in the experiment. This assertion is supported by the qualitative agreement between experimental observations and theoretical predictions.

REFERENCES

Aref, H. 1984 Stirring by chaotic advection. *J. Fluid Mech.* **143**, 1–21.

Aref, H. & Balachandar, S. 1986 Chaotic advection in Stokes flow. *Physics Fluids* **29**, 3515–3521.

Bau, H. H., Zhong, J. & Yi, M. 2001 A minute magneto hydro dynamic (MHD) mixer. *Sensors and Actuators* B **79**/2–3, 205–213.

Brinkman, H. C. 1947 A calculation of the viscous force exerted by a flowing fluid on a dense swarm of particles. *Appl. Sci. Res.* A **1**, 27.

Chaiken, J., Chevray, R. K., Tabor, M. & Tan Q. M. 1986 Experimental study of Lagrangian turbulence in Stokes flow. *Proc. R. Soc. Lond.* A **408**, 165–174.

Chaiken, J., Chu, C. K., Tabor, M. & Tan Q. M. 1987 Lagrangian turbulence and spatial complexity in Stokes flow. *Phys. Fluids* **30**, 687–694.

Davidson, P. A. 2001 *An Introduction to Magnetohydrodynamics*. Cambridge University Press.

Fernandez, J., Kurowski, P., Petitjeans, P. & Meiburg, E. 2002 Density-driven unstable flows of miscible fluids in a Hele-Shaw cell. *J. Fluid Mech.* **451**, 239–260.

Grassberger, P. & Procaccia, I. 1983 On the characterization of strange attractors. *Phys. Rev. Lett.* **50**, 346–349.

Jang, J. & Lee, S. S. 2000 Theoretical and experimental study of MHD (magnetohydrodynamic) micropump. *Sensors and Actuators* A **80**, 84–89.

Jeffery, G. B. 1922 The rotation of two circular cylinders in viscous fluid. *Proc. R. Soc. Lond.* A **101**, 169–174.

Landau, L. D. & Lifshitz, E. M. 1959 *Fluid Mechanics*. Pergamon.

Lemoff, A. V. & Lee, A. P. 2000 An AC magnetohydrodynamic micropump. *Sensors and Actuators* B **63**, 178–185.

Levich, V. G. 1962 *Physiochemical Hydrodynamics*. Prentice Hall.

Meleshko, V. V. & Aref, H. 1996 A blinking rotlet model for chaotic advection. *Phys. Fluids* **8**, 3215–3217.

Moon, P. & Spencer, D. E. 1971 *Field Theory Handbook*. Springer.

Ottino, J. M. 1989 *The Kinematics of Mixing: Stretching, Chaos, and Transport*. Cambridge University Press.

White, F. M. 1974 *Viscous Fluid Flow*. McGraw Hill.

Wolfram, S. 1996 *Mathematica*. Cambridge University Press.

Woodson. H. H. & Melcher, J. R. 1969 *Electromechanical Dynamics*, Vol. III. John Wiley.

Yih, C.-S. 1979 *Fluid Mechanics*. West River Press.

Zhong, J., Yi, M. & Bau, H. H. 2002 A magneto-hydrodynamics (MHD) pump fabricated with ceramic tapes. *Sensors and Actuators* A **96**, 59–66.